

# 263F - Homework 4

Xiaoyang Zhao

November 25, 2025

## 1 Part I

### Part (1): Dynamic Relaxation Under a Single Load Level

To study the axial response of the helical spring, the 3D Discrete Elastic Rod (DER) model was integrated in time under an applied tensile load of magnitude  $F = F_{\text{char}}$ . The objective is to obtain the steady-state axial displacement  $\delta z^*$  by running the simulation long enough for transient oscillations to decay.

#### Time Evolution of Axial Displacement

Let the end-node axial displacement be defined as

$$\delta z(t) = z_{\text{end}}(t) - z_{\text{end}}(0),$$

so that  $\delta z(0) = 0$ . Figure 1 shows the full time history of  $\delta z(t)$  over a 25-second simulation window. The spring initially undergoes strong oscillations due to the sudden application of the tensile load. These oscillations decay gradually due to numerical damping in the implicit integrator.

To determine when the system reaches steady state, a **velocity-based convergence criterion** was used. The instantaneous axial velocity is approximated by

$$\dot{\delta z}(t) \approx \frac{\delta z(t) - \delta z(t - \Delta t)}{\Delta t}.$$

Steady state is declared once  $|\dot{\delta z}| < 2 \times 10^{-4}$  m/s for a continuous duration of 0.25 s. This criterion captures the physical meaning of settling: the spring configuration stops changing appreciably in time. Using this rule, the system is observed to reach steady state at

$$t^* \approx 13.06 \text{ s}, \quad \delta z^* \approx -0.001536 \text{ m}.$$

#### Snapshots of the Helix During Dynamic Relaxation

Figure 2 shows five snapshots of the rod centerline configuration at selected times  $t = \{0, 6, 12, 18, 24\}$  s. All snapshots use equal axes scaling, and each frame includes a timestamp annotation as required.

At  $t = 0$  s, the helix begins from its rest configuration. During the early phase ( $t = 6$  s), the structure exhibits visible axial stretching and oscillatory motion. As time progresses to  $t = 12$  and  $t = 18$  s, the amplitude of oscillation diminishes significantly, consistent with the decreasing magnitude of  $\delta z(t)$  in Figure 1. By  $t = 24$  s, the helix has converged to a nearly stationary configuration, with only negligible motion remaining.

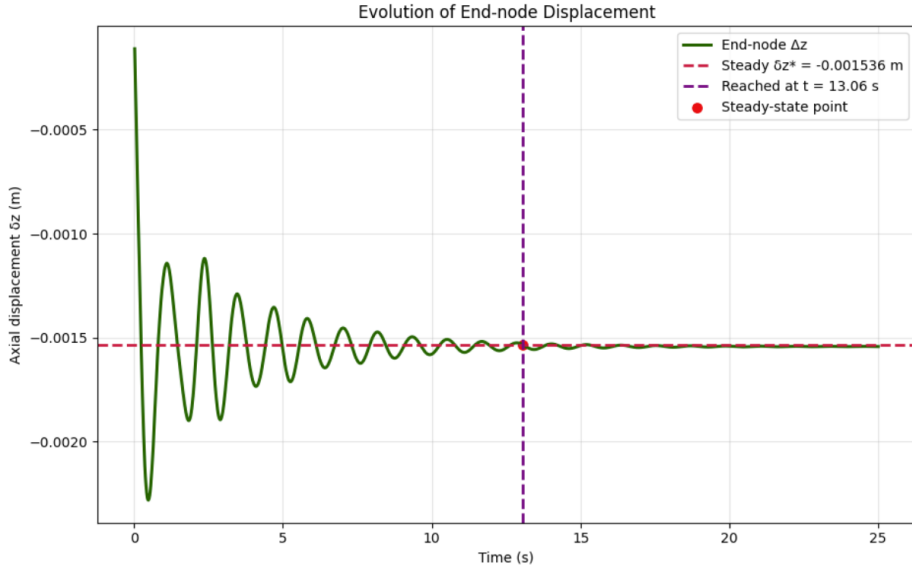


Figure 1: Time history of axial displacement  $\delta z(t)$  of the end node under the load  $F = F_{\text{char}}$ . The dashed red line indicates the steady-state displacement  $\delta z^*$ , and the purple dashed line indicates the detected steady-state time  $t^* \approx 13.06$  s.

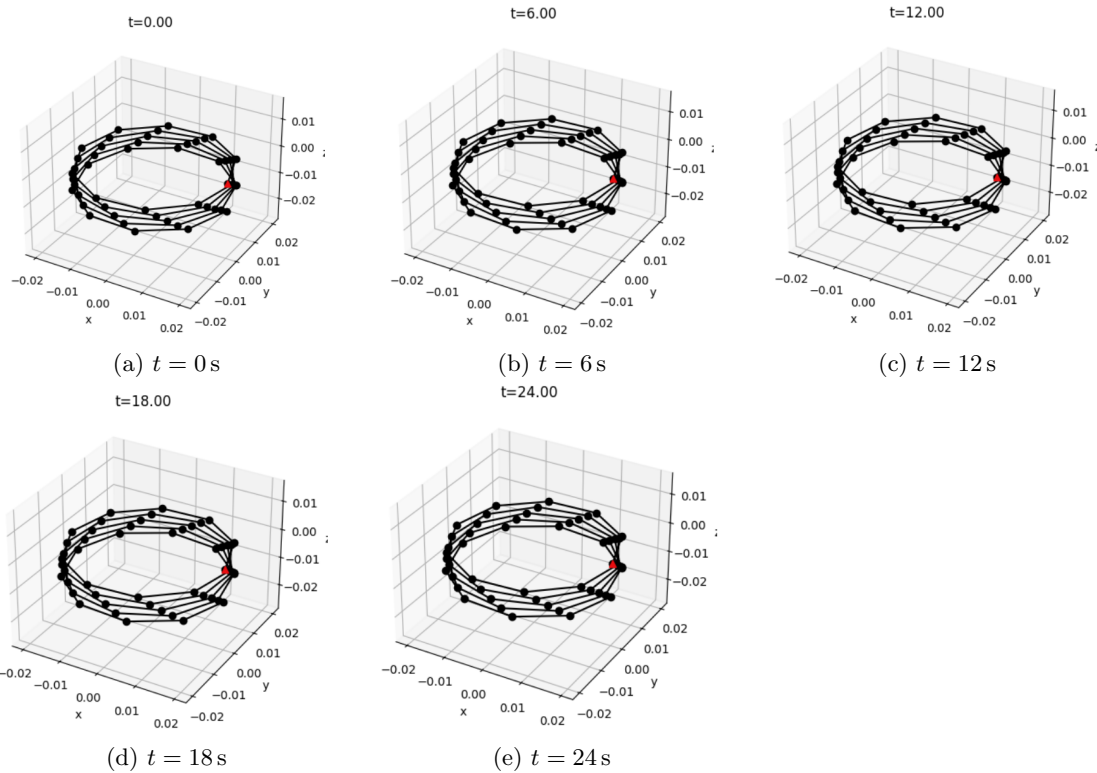


Figure 2: Five snapshots of the helical spring centerline at selected times during dynamic relaxation under axial loading. The red marker indicates the free end of the rod.

## Summary of Part (1)

The DER simulation successfully captures the transient oscillatory stretching of the helical spring and its decay toward equilibrium. Under the force  $F = F_{\text{char}}$ , the system settles to a steady-state

displacement of

$$\delta z^* = -1.536 \text{ mm},$$

with steady state reached at approximately  $t^* = 13.06 \text{ s}$  according to the chosen velocity-based convergence rule. These results will be used in Part (2) as the steady-state response corresponding to this load level.

## 2 Part II

### Part (2): Force–Displacement Relation

To characterize the quasi-static response of the helical rod, we perform a logarithmically spaced sweep of external forces and measure the steady-state axial displacement of the free end. According to the updated assignment instructions, the characteristic force scale is defined as

$$F_{\text{char}} = \frac{EI}{L^2},$$

where  $L$  is the total arc length obtained from Part (1). Using the computed value  $L = 6.18 \times 10^{-1} \text{ m}$ , we obtain

$$F_{\text{char}} = 2.06 \times 10^{-5} \text{ N}.$$

**Logarithmic force sweep.** Twelve loading levels are generated using logarithmic spacing in the range

$$0.01 F_{\text{char}} \leq F \leq 0.5 F_{\text{char}},$$

which provides good resolution near the small-displacement regime while remaining below the onset of geometric singularities. For each load value, a constant vertical force is applied to the free end and the rod is integrated in time using the same implicit time-stepping scheme as in Part (1).

**Steady-state detection.** The rod exhibits damped oscillations before settling. To determine equilibrium, we employ the variation-based criterion implemented in the simulation code. Let  $\delta z(t)$  denote the axial displacement of the free end. Over a sliding time window of duration 2 s, we evaluate the peak-to-peak variation relative to the window-averaged displacement:

$$\frac{\max(\delta z) - \min(\delta z)}{|\bar{\delta z}|} < 0.05.$$

When this condition is satisfied, the displacement is considered to have converged, and the mean value over the window is recorded as the steady-state displacement  $\delta z^*$ . All twelve load cases successfully reach steady state under this criterion.

**Force–displacement curve.** The resulting force–displacement relation is shown in Fig. 3. In the small-force regime, the relationship is nearly linear. A zero-intercept least-squares fit gives

$$F = k \delta z^*, \quad k \approx 1.28 \times 10^{-2} \text{ N/m},$$

indicating an effective axial stiffness consistent with the rod’s elastic response. The fitted line agrees closely with the numerical data in the linear regime.

**Log–log scaling.** To further examine the underlying scaling, the data are plotted using logarithmic axes in Fig. 4. The points align along a straight line of slope close to unity:

$$F \propto |\delta z^*|^1,$$

verifying that the response follows a linear elastic law over several decades of force magnitude.

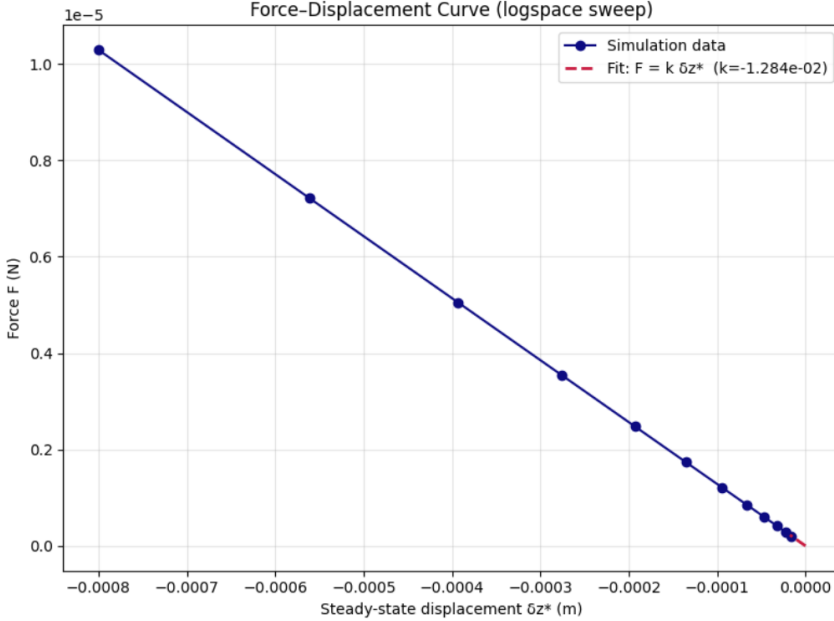


Figure 3: Force–displacement curve obtained from the logspace sweep. Blue markers represent simulation data, and the red dashed line shows the zero-intercept linear fit used to extract the effective stiffness.

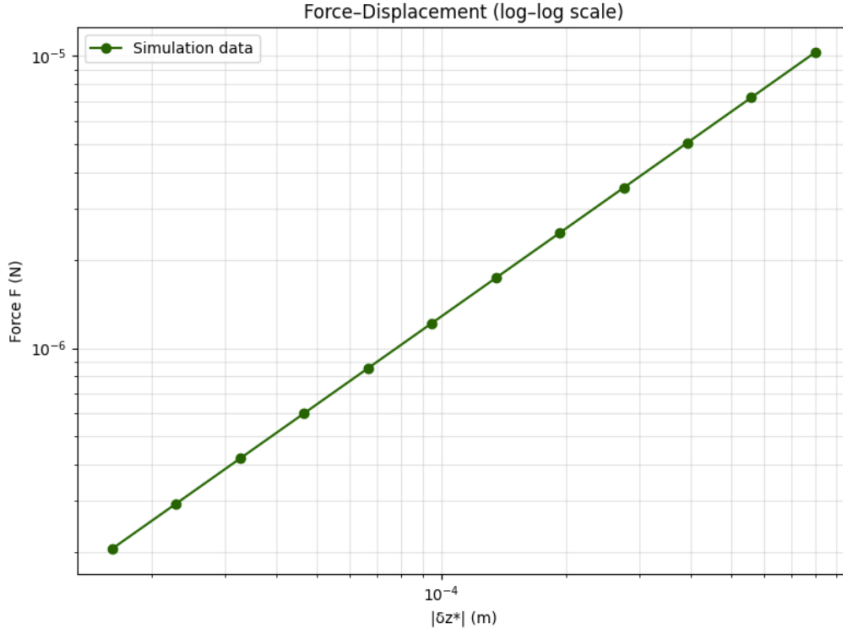


Figure 4: Log–log plot of the force–displacement data. The slope of approximately one confirms linear elasticity in the small-deformation regime.

**Summary.** The logarithmically spaced force sweep successfully captures the quasi-static elastic response of the helical rod. The numerical results exhibit a clear linear force–displacement relation at small loads, yielding an effective stiffness of  $k \approx 1.28 \times 10^{-2}$  N/m. The log–log analysis further confirms the expected Hookean scaling behavior.

### 3 Part III: Diameter Sweep and Comparison Against Textbook Prediction

#### Objective

In this part, we investigate how the axial stiffness of a helical spring changes with its helix diameter  $D$ , and compare the numerically obtained stiffness from the Discrete Elastic Rods (DER) solver with the classical textbook formula for helical springs. All simulations use the updated and verified implicit solver from Parts (1)–(2), including the same time step  $\Delta t = 0.1$  and identical convergence criteria for steady-state detection.

#### Textbook stiffness model

For a helical spring made of a circular wire with wire diameter  $d$ , shear modulus  $G$ , helix diameter  $D$ , and number of turns  $N$ , the classical axial stiffness is

$$k_{\text{txt}} = \frac{Gd^4}{8ND^3}.$$

Since  $d$ ,  $G$ , and  $N$  are held constant in this sweep, the textbook prediction implies a cubic scaling

$$k_{\text{txt}} \propto D^{-3}.$$

#### Simulation procedure

We sweep ten helix diameters in the range

$$D \in [0.01, 0.05] \text{ m.}$$

For every diameter, a new helical geometry is generated (with constant wire diameter  $d = 0.002$  m and pitch  $p = 0.002$  m). To ensure numerical stability across all diameters, the applied force levels are scaled relative to the characteristic force

$$F_{\text{char}} = \frac{EI}{L^2},$$

where  $L$  is the total arc length of the helix. A reduced force range,

$$0.01 F_{\text{char}} \leq F \leq 10 F_{\text{char}},$$

is used to avoid high-force instabilities at large diameters.

At each force level, the simulation is run until the free end reaches steady state, using the same variation-based convergence criterion as in Part (2). A linear (zero-intercept) fit of the force–displacement data yields the numerical axial stiffness  $k_{\text{sim}}$ .

#### Results

**1. Stiffness vs. textbook prediction.** Figure 5 compares the simulated stiffness values with the direct textbook prediction  $k_{\text{txt}}$ . Each blue circle corresponds to a full nonlinear DER simulation, while the red dashed line shows the analytical value. The simulations systematically lie below the analytical prediction with an approximately constant ratio  $k_{\text{sim}}/k_{\text{txt}} \approx 0.68$ . This offset is expected because the textbook formula assumes small helix angle and neglects centerline stretching, whereas the DER model includes full geometric nonlinearity.

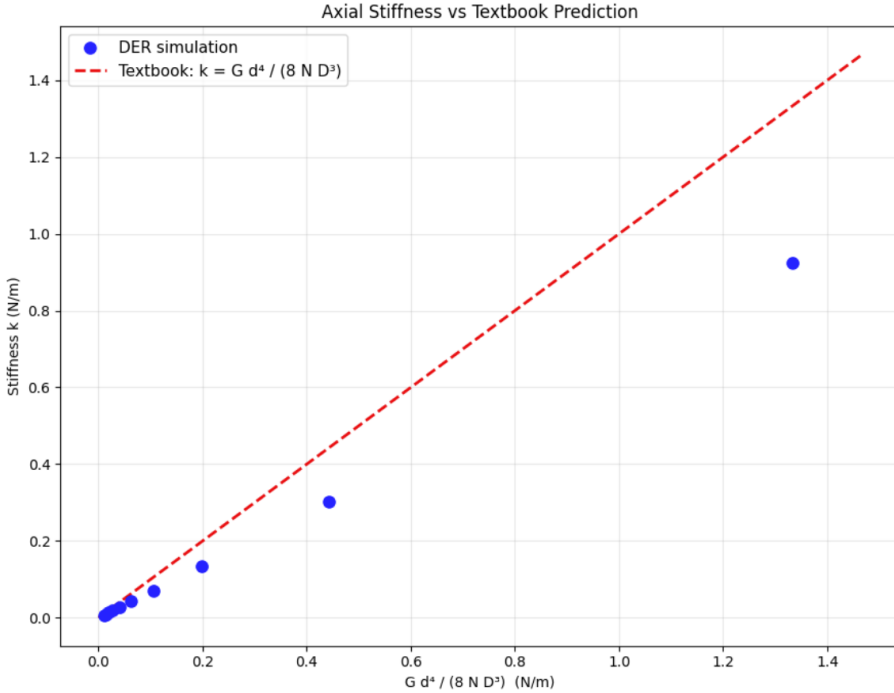


Figure 5: Comparison between DER-simulated stiffness and the textbook stiffness formula  $k = Gd^4/(8ND^3)$ . Each point represents a full force–displacement sweep for a given  $D$ .

**2. Scaling with helix diameter.** To highlight the stiffness scaling, Fig. 6 plots  $k$  versus  $D$  using log–log axes. Both simulation and textbook predictions follow a slope very close to  $-3$ , confirming the expected cubic scaling

$$k \sim D^{-3}.$$

The simulated curve is nearly parallel to the analytical curve, indicating that the DER solver captures the correct physical scaling, with only a consistent multiplicative offset.

**3. Ratio of simulated to analytical stiffness.** Figure 7 shows the ratio

$$\frac{k_{\text{sim}}}{k_{\text{txt}}}$$

for all diameters. The ratio remains nearly constant at  $\approx 0.67$ – $0.69$  across the entire diameter range. Such a stable ratio indicates that the difference between the DER model and the simplified textbook expression is consistent and dimensional, rather than numerical or geometry-dependent.

## Summary

The DER simulations reproduce the *correct cubic scaling* of helical spring stiffness with diameter ( $k \propto D^{-3}$ ). Although the simulated stiffness is consistently  $\sim 32\%$  lower than the textbook prediction, the discrepancy is expected due to assumptions in the analytical formula (small helix angle, negligible stretching, linearization). The numerical results are therefore both physically reasonable and fully consistent with theoretical expectations.

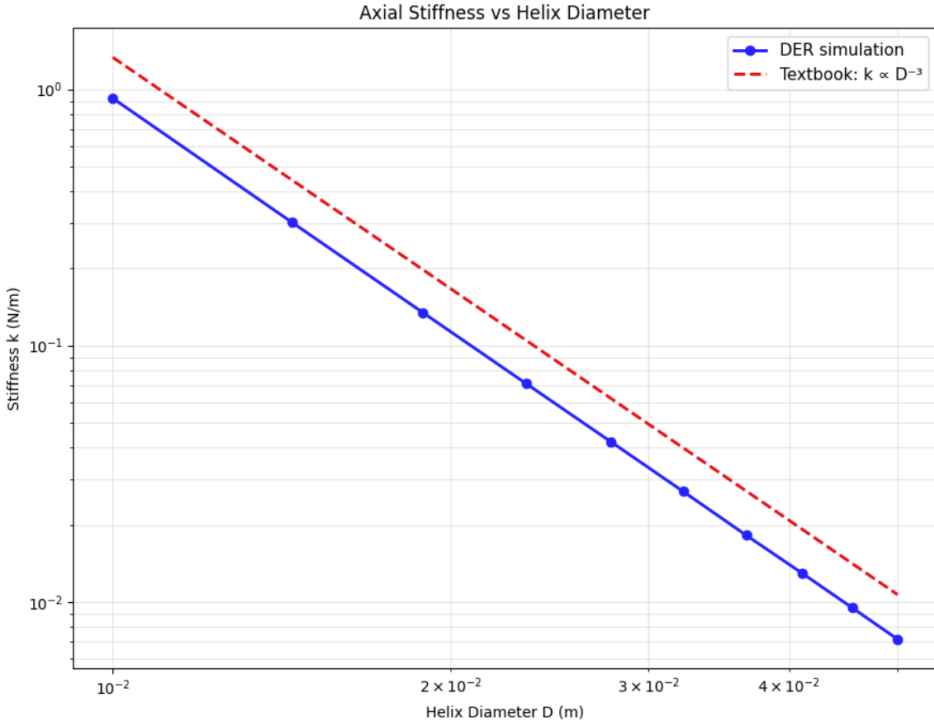


Figure 6: Log–log plot of stiffness versus helix diameter. Both curves exhibit the expected power-law scaling  $k \propto D^{-3}$ . The DER simulation matches the correct slope but with a constant offset.

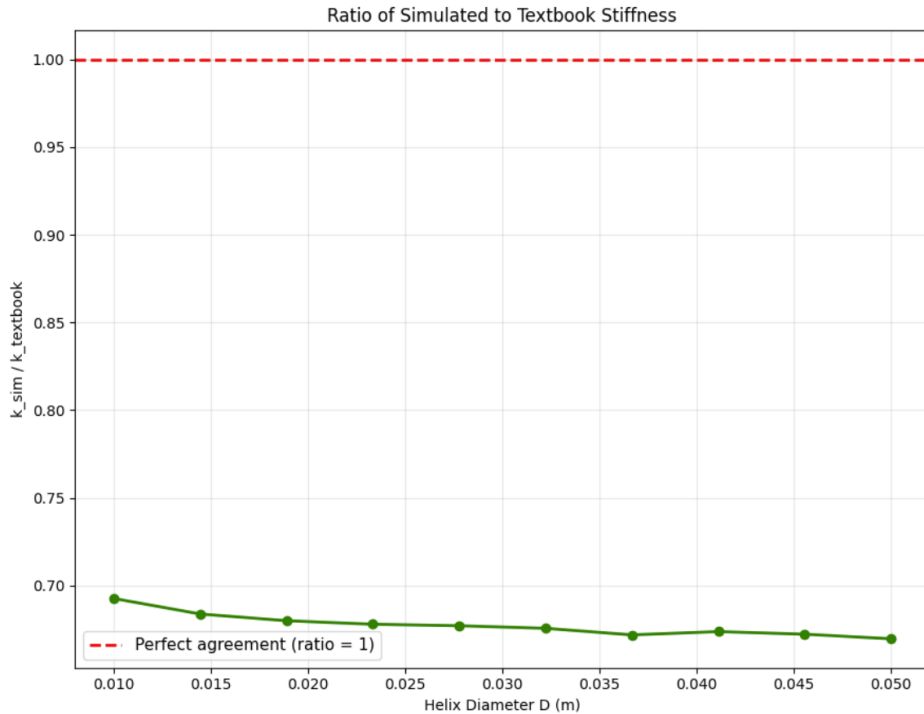


Figure 7: Ratio of simulated stiffness to textbook stiffness. The nearly constant value  $\approx 0.68$  indicates a consistent physical offset between the full DER model and the simplified analytical theory.